

Special Collection:

The Arctic Ocean's changing
Beaufort Gyre

Key Points:

- A numerical 3-layer model is used to study instability and eddy dynamics over the continental slope in an idealized wind-driven ocean gyre
- Eddy fluxes of potential vorticity are down-gradient in all three layers
- Linearized stability calculations are able to reproduce the qualitative features of PV fluxes near the slope

Correspondence to:

P. E. Isachsen,
p.e.isachsen@geo.uio.no

Citation:

Isachsen, P. E., Vogt-Vincent, N. S., Johnson, H. L., & Nilsson, J. (2024). Instability and mesoscale eddy fluxes in an idealized 3-layer Beaufort Gyre. *Journal of Geophysical Research: Oceans*, 129, e2023JC020757. <https://doi.org/10.1029/2023JC020757>

Received 27 NOV 2023

Accepted 27 JUL 2024

Author Contributions:

Conceptualization: Pål E. Isachsen, Helen L. Johnson

Formal analysis: Pål E. Isachsen, Noam S. Vogt-Vincent, Helen L. Johnson, Johan Nilsson

Investigation: Pål E. Isachsen, Noam S. Vogt-Vincent, Helen L. Johnson, Johan Nilsson

Methodology: Pål E. Isachsen

Software: Pål E. Isachsen

Visualization: Pål E. Isachsen, Noam S. Vogt-Vincent

Writing – original draft: Pål E. Isachsen

Writing – review & editing: Pål E. Isachsen, Noam S. Vogt-Vincent, Helen L. Johnson, Johan Nilsson

© 2024. The Author(s).

This is an open access article under the terms of the [Creative Commons](#)

Attribution-NonCommercial-NoDerivs License, which permits use and

distribution in any medium, provided the original work is properly cited, the use is non-commercial and no modifications or adaptations are made.

Instability and Mesoscale Eddy Fluxes in an Idealized 3-Layer Beaufort Gyre

Pål E. Isachsen^{1,2} , Noam S. Vogt-Vincent³ , Helen L. Johnson³ , and Johan Nilsson⁴ 
¹Department of Geosciences, University of Oslo, Oslo, Norway, ²Norwegian Meteorological Institute, Oslo, Norway,

³Department of Earth Sciences, University of Oxford, Oxford, UK, ⁴Department of Meteorology, Stockholm University, Stockholm, Sweden

Abstract We study the impacts of a continental slope on instability and mesoscale eddy fluxes in idealized 3-layer numerical model simulations. The simulations are inspired by and mimic the situation in the Arctic Ocean's Beaufort Gyre, where anti-cyclonic winds drive anti-cyclonic currents that are guided by the continental slope. The forcing and currents are retrograde with respect to topographic Rossby waves. The focus of the analysis is on eddy potential vorticity (PV) fluxes and eddy-mean flow interactions under the Transformed Eulerian Mean framework. Eddy lateral vorticity fluxes dominate over the continental slope where eddy form stress, that is, vertical momentum flux, is suppressed due to the topographic PV gradient. The diagnosis also shows that while eddy momentum fluxes are up-gradient over parts of the slope, the total quasi-geostrophic PV flux is down-gradient everywhere. We then calculate the linearly unstable modes of the time-mean state and find that the most unstable mode contains several key features of the observed finite-amplitude fluxes over the slope, including down-gradient PV fluxes. When accounting for additional unstable modes, more qualitative features of the observed eddy fluxes in the numerical model are reproduced.

Plain Language Summary The ocean circulation in the Arctic is heavily influenced by the bottom bathymetry. Essentially, currents are steered to follow continental slopes and submarine ridges. This topographic steering makes transfer of properties by ocean currents across continental slopes difficult, and the result is that the deep basins are partially isolated from the continental shelves. Large-scale oceanic turbulence, or “mesoscale eddies,” are able to cross bottom bathymetry, but transport by such eddies is also hampered. In this study, a simplified numerical model is used to learn about how bottom bathymetry impacts eddy transport in and out of the Beaufort Gyre, a wind-driven large-scale gyre in the Arctic Ocean's Canada Basin. The gyre is the largest reservoir of fresh waters in the Arctic, and understanding how topography controls the export of this freshwater is thought to be of crucial importance if climate models are to properly simulate a future Arctic Ocean. The study shines light on some key aspects that the models need to capture to get transport across the continental slope right.

1. Introduction

The large-scale ocean currents at high northern latitudes are heavily guided by bottom bathymetry (Koszalka et al., 2011; Nøst & Isachsen, 2003; Orvik & Niiler, 2002). Certainly, the geostrophically-balanced bottom currents need to be quite topographically aligned. This is because the weak planetary vorticity gradient at high latitudes leaves the geostrophic flow nearly divergentless. This, in turn, means that the bottom vertical velocity—set up by flow up or down bathymetric slopes—must be the same order of magnitude as the vertical velocity at the sea surface, which is very small indeed (Cushman-Roisin & Beckers, 2011). The north polar oceans are also less stratified than at lower latitudes (Rudels & Carmack, 2022). In the unstratified f-plane limit, the geostrophic flow is vertically rigid, moving as so-called Taylor-Proudman columns (G. K. Vallis, 2017), so surface currents also align with topography. With finite stratification, currents further up in the water column are less constrained. But rotation of the thermal wind shear away from the bottom flow does require a non-trivial organization of vertical velocities or ageostrophic buoyancy transport (Schott & Stommel, 1978; Schott & Zantopp, 1980). So, in practice, even surface currents typically feel the continental slopes and ridge systems thousands of meters below.

The strong topographic steering of the large-scale geostrophic flow field then raises the question of what processes are responsible for transport of water tracers and suspended material across topographic gradients. Understanding this is key for piecing together how, for example, continental shelves are connected to the various

deep ocean basins that define the Arctic. The mesoscale eddy field has been identified as a key player, at least in the Nordic Seas where eddy fluxes appear to be crucial in closing heat and freshwater budgets (Isachsen & Nøst, 2012; Isachsen et al., 2012; Segtnan et al., 2011; Spall, 2010; Ypma et al., 2020). In the Arctic Ocean proper, mesoscale eddies are abundant in observations (an overview is given by Timmermans & Marshall, 2020), but their net impacts on large-scale property budgets has been somewhat less studied.

One notable exception is the Beaufort Gyre, a large-scale flow feature in the Canada Basin of the Arctic Ocean. Here, anti-cyclonic winds drive a surface Ekman convergence of freshwater toward the center of the basin. This lifts the sea surface and pushes down isopycnals, driving anti-cyclonic geostrophic currents near the surface and, at the same time, a thermal wind shear that reduces these currents at depth (Proshutinsky et al., 2002). The mass accumulation from the convergent surface Ekman transport may be compensated by divergent bottom Ekman currents, so that one can envision an Eulerian secondary overturning circulation through the gyre, inward at the surface, downward in the center of the gyre and outward at the bottom (Manucharyan & Isachsen, 2019). An alternative interpretation of the role of bottom friction is that it passes the wind momentum into the solid ground below the gyre, as in Gill's model of the Antarctic Circumpolar Current (A. Gill, 1968).

In steady state, some of the downward Ekman pumping in the center of the gyre may be associated with diapycnal flow allowed by irreversible water mass transformation due to local air-sea-ice fluxes and small-scale turbulent mixing (Zhang & Steele, 2007). However, under the sheltering effect of the sea ice cover, water mass transformation is generally found to be modest compared to oceans at lower-latitude (Timmermans & Marshall, 2020). In an alternative view, much of the Ekman-driven overturning circulation in the Beaufort Gyre is instead compensated by adiabatic mesoscale eddy transport. Essentially, the available potential energy (APE) field associated with the inclined density field drives baroclinic instability and an eddy-driven overturning, which is thought to counter the wind-driven overturning circulation. It is the sum of these two opposing overturning cells, the “residual” circulation, which advects tracers in and out of the gyre (Davis et al., 2014; Manucharyan & Spall, 2016; Manucharyan et al., 2016; Meneghello et al., 2017). The eddy overturning can be cast in terms of lateral buoyancy fluxes or, alternatively, in terms of eddy form stresses that transfer the wind momentum down through the stratified water column (Johnson & Bryden, 1989). On seasonal timescales, the surface Ekman transport is modulated by the sea ice motion in what has been termed the “ice-ocean governor” (Meneghello et al., 2018). However, integrated over long timescales, and in the limit of weak small-scale mixing, the lowest-order dynamics of the gyre appears to be reflecting this relatively simple balance between the opposing wind-driven and eddy-driven overturning circulations.

A potential problem with this model of Ekman-eddy residual overturning circulation arises from the fact that baroclinic instability and eddy buoyancy fluxes may be severely hampered by the presence of continental slopes that confine the Beaufort Gyre. In essence, topographic potential vorticity (PV) gradients can be expected to hinder any cross-bathymetric flow, be it large-scale or mesoscale (Sterl et al., 2024). A natural starting point for considering topographic impacts on baroclinic instability is the “topographic Eady model” of Blumsack and Gierasch (1972). This model, in which a linear bottom slope is added to the Eady model of baroclinic instability, predicts reduced growth rates and generally also reduced length scales over sloping bathymetry. However, this model generally overestimates topographic suppression when tested in realistic situations (Trodahl & Isachsen, 2018). Key limitations of the Eady framework itself include its inability to account for internal PV thickness gradients in the middle of the water column as well as relative vorticity gradients and associated momentum and vorticity fluxes.

The second of these two limitations appears to be most severe over continental slopes, as suggested by two idealized numerical studies of wind-driven flows over continental slopes by Wang and Stewart (2018) and Manucharyan and Isachsen (2019), hereafter referred to as WS18 and MI19, respectively. Both studies focused on so-called retrograde flows, where the winds drive currents that are in the opposite direction to topographic waves (such waves have the coast to their right in the northern hemisphere). The MI19 study was motivated specifically by the Arctic Ocean Beaufort Gyre—whose anti-cyclonic mean flow is retrograde. These numerical studies confirm that eddy form stress, that is, the vertical transfer of momentum which is a signature of active baroclinic instability, is greatly reduced over the continental slope. What the eddy field instead does in both of these simulations is to transfer momentum laterally in the surface layers, away from the slope region and to a location just off the slope where the bottom is relatively flat. Here, an eddy driven jet is formed. This jet is then baroclinically unstable, allowing the wind momentum to finally be transferred to the solid ground below.

Thus, both studies indicate that lateral momentum fluxes play an important role over continental slopes. However, the findings also left some unanswered questions. First, the lateral momentum fluxes over the slope in these models were not down-gradient everywhere, so the eddy field was not the result of pure barotropic instability in the upper layers. In both sets of simulations, there was also some indication of reversed eddy buoyancy fluxes and the formation of prograde flows over the lower parts of the slope. Thus, the mesoscale dynamics, at least over idealized retrograde slopes, appears to be associated with regions of both up-gradient buoyancy fluxes and up-gradient momentum fluxes. WS18 tried to interpret the observed behavior in their channel simulation in terms of down-gradient PV fluxes, to connect with theories of eddy-driven jets along topography (e.g., Bretherton & Haidvogel, 1976; G. Vallis & Maltrud, 1993). Doing the analysis along a set of mid-depth isopycnals, they indeed found down-gradient PV fluxes over the slope regions. However, the same diagnostics gave indications of up-gradient PV fluxes in other parts of their model domain, notably over the flat continental shelf and deep basin. Whether this somewhat complex behavior is a real dynamical feature or an artifact of their analysis method remains unanswered.

Second, one wonders how the observed finite-amplitude eddy fluxes relate to the stability properties of the equilibrated time-mean flow. More specifically, can the observed fluxes be explained, at least qualitatively, by the eigenvectors of the linearly unstable modes of the time-mean flow? For this to be the case, the time-mean flow will have to be only weakly unstable so that eddy-eddy interactions do not produce a deep inverse energy cascade that take eddy characteristics away from the linear prediction (Jansen & Ferrari, 2012). Several studies suggest that the mid-latitude atmosphere tends to adjust toward such a weakly-unstable regime, where the morphology of the macroturbulence bears some resemblance to the predictions of the linearized calculations (e.g., Lindzen, 1993; Schneider & Walker, 2006; Stone, 1978). The issue is often discussed in terms of the criticality of baroclinic flows on a beta plane in the quasi-geostrophic (QG) 2-layer Phillips model. For that problem, the criticality parameter can be cast as

$$\xi = \frac{f s_i}{H \beta}, \quad (1)$$

where f and β are the Coriolis parameter and its meridional gradient, respectively, H is the troposphere thickness and s_i is the slope of the isentropes. Marginal criticality in this system means that planetary beta cancels the PV thickness gradient in the lower layer, thus violating the Charney-Stern-Pedlosky necessary criterion for onset of instability (see e.g. G. K. Vallis, 2017). Alternatively, since thermally-sheared westerlies are retrograde with respect to planetary baroclinic Rossby waves, one can recast the criticality as

$$\xi = \frac{U}{\beta L_d^2}, \quad (2)$$

where U is the thermal wind shear and $L_d = NH/f$ is the internal deformation radius (with buoyancy frequency N given by the vertical density stratification). Hence, the criticality in this idealized QG system can also be viewed as the ratio of the thermal wind velocity and the speed of long internal planetary Rossby waves (βL_d^2). Finally, if the thermal wind shear gives an indication of the macroturbulent velocity magnitude, Equation 2 can be viewed as the (squared) ratio between a Rhines length scale ($\sqrt{U/\beta}$; Rhines, 1975) and the deformation radius. If the inverse cascade is arrested at the Rhines scale, then ξ measures the potential expansion in size of deformation-scale eddies (the approximate scale of fastest growth in the 2-layer Phillips model; see e.g. G. K. Vallis, 2017).

Even though numerous studies, starting with A. E. Gill et al. (1974), have investigated linear baroclinic instability in the ocean, the evidence for marginal criticality there is much less clear. Arguments have also been made that the ocean is typically supercritical with respect to baroclinic Rossby waves, essentially because a weaker stratification and smaller vertical scale than in the atmosphere results in an internal deformation radius that is generally small compared to the Rhines scale (see e.g. Jansen & Ferrari, 2012). Estimates of energy spectral fluxes in the ocean, both from observations and models, also generally suggest the presence of modest inverse cascades (Scott & Wang, 2005; Tulloch et al., 2011). Except for the Antarctic Circumpolar Current, however, ocean currents generally bear little resemblance to the mid-latitude atmospheric westerlies. Moreover, at the latitudes covered by the Arctic Ocean—where the gradient of the Coriolis parameter becomes very small—the assessment of criticality with respect to planetary Rossby waves is likely not of much relevance.

And yet, since the Beaufort Gyre is retrograde with respect to *topographic* Rossby waves, the above criticality measures may become useful if one replaces planetary beta with topographic beta $\beta_t = (f/H)s_t$ where s_t is the topographic slope. The relevant criticality parameter then becomes

$$\xi = \frac{s_i}{s_t}, \quad (3)$$

which turns out to be the inverse of the δ parameter that controls instability in the modified Eady model of Blumsack and Gierasch (1972). MI19 showed gridded hydrographic data from the Beaufort Gyre (their Figure 1) which indicate that the continental slope is steeper than isopycnals over much of the gyre, suggesting that the time-mean flow may even be in a subcritical regime. Of course, the above criticality measure is based on a simplified theory of pure baroclinic instability, notably one which ignores the lateral shear of the flow. It nonetheless gives some indication that the flow in the gyre may in fact be somewhere near a criticality threshold—in which case it will make sense to investigate whether linear stability calculations can teach us something about the observed eddy field.

MI19 did not assess stability in their idealized Beaufort Gyre simulations, but WS18 did so for their topographically-retrograde channel simulations, using a QG 1D vertical mode approach (Smith, 2007). In these analyses, which can identify instability due to the local vertical structure of the time-mean stratification and flow field (i.e., pure baroclinic instability), they observed clear indications of topographic suppression of growth rates—as well as enhanced growth rates over flat regions offshore. However, due to the limitations of the 1D framework used, they could not account for any potential effects of background lateral vorticity gradients. They could therefore also not investigate whether the linearly unstable modes contain a signature of the lateral momentum fluxes observed in their non-linear model fields. As such, their conclusions regarding linear instability and its relationship to the dynamics of the simulated macro turbulent flow must be considered preliminary.

The present study continues from the work of WS18 and MI19 by examining more closely the dynamics of eddy fluxes and their relation to linear stability properties over retrograde continental slopes. To focus on the core issues, we simplify the approach and study nonlinear fluxes as well as linear stability in a 3-layer context, in a circular basin that crudely represents conditions in the Beaufort Gyre. By reducing the vertical resolution so drastically, we limit the types of instability which may be reproduced, for example, preventing surface-trapped small-scale eddy growth, which is frequently observed in the Arctic Ocean halocline (e.g., Zhao et al., 2014). What the model will be able to represent, however, are the larger mesoscale eddies responsible for the deep overturning circulation in the basin and, it can be argued, for the adjustment of the main halocline (the adjustment of the density interface of a two-layer system will require a deep overturning). That such an eddy field should exist has been suggested by stability calculations from real hydrographic profiles (Meneghello et al., 2021) and also by recent satellite-based observations (Kubryakov et al., 2021). We nonetheless incorporate three layers instead of two, to allow for an examination of impacts from internal PV gradients, if there are any.

The specific issues to be addressed in this idealized 3-layer study are (a) the impact of a retrograde continental slope on PV fluxes, including an investigation into PV diffusivities, and (b) the relationship between the observed fluxes and the linearly unstable modes of the background state in the model. To examine both lateral and vertical momentum exchanges by unstable modes, we study linear stability in a 2D context—in a plane crossing the mean hydrography and mean flow. As will be seen, even under the extreme simplification of three layers, the linear calculation is able to qualitatively reproduce key features observed in the full-complexity primitive equation studies mentioned above.

The manuscript starts with a description of the numerical model and the linear stability algorithm. The main results are then organized into a first part describing and analyzing the fully non-linear fields, and a second part discussing the linear stability of the flow. The study concludes with a brief discussion of the obtained results.

2. Methods

2.1. Numerical Model Simulations

The model used is Aronnax (Doddridge & Radul, 2018), an open-source non-linear isopycnal model with an explicit free surface, formulated on a staggered C-grid. In this study, the model is set up on an f-plane (a

reasonable approximation at the high latitudes of the Beaufort Gyre) with Coriolis parameter $f = 1.46 \times 10^{-4} \text{ s}^{-1}$, the value at 90°N . The domain consists of a circular basin of radius 750 km representing the Beaufort Gyre and a rectangular “nudging channel” of dimensions $500 \times 500 \text{ km}$ meant to represent a connection to hydrographic conditions outside of the gyre. In the nudging region, layer thicknesses are relaxed toward reference values (see below) with a timescale of 0.1 days. The very short nudging timescale ensures that thickness anomalies generated by the slope and basin dynamics are washed out within the nudging region.

A linear continental slope is used. In the model's Beaufort Gyre, that is, in the circular basin, the total depth H is defined as:

$$H(r) = H_0 + H_1 \cdot \min\left(\frac{R-r}{L_s}, 1\right), \quad (4)$$

where r is the radial distance from the gyre center, R is the gyre radius (750 km), L_s is the horizontal extent of the continental slope (variable, depending on the experiment; see below), H_0 is the minimum depth (500 m) and H_1 is the height of the slope (3,500 m). The nudging channel has the same slope steepness but a rectangular geometry. Finally, we add random noise of root-mean-square amplitude 20 m to the bathymetry to help instigate instability.

The model has three isopycnal layers with interface reduced gravities $g'_{12} = g(\rho_2 - \rho_1)/\rho_0 = 0.024 \text{ m s}^{-2}$ and $g'_{23} = g(\rho_3 - \rho_2)/\rho_0 = 0.008 \text{ m s}^{-2}$. The resting layer thicknesses of the two top layers are 80 and 120 m, respectively, while the thickness of the third layer varies over the continental slope but is 3,800 m in the center basin. These values are loosely based on the basin-margin T-S profiles from Lique et al. (2015) and also correspond fairly closely with the 3-layer model configuration of the central Arctic by Manucharyan and Stewart (2022).

The horizontal resolution is set to 5 km, compared to a first baroclinic deformation radius in the central basin of about 11.5 km in all experiments. There is no explicit interface friction or diapycnal volume transport between layers, but the simulations use a harmonic lateral friction coefficient of size $15 \text{ m}^2 \text{ s}^{-1}$, no-slip lateral boundary conditions and a linear bottom drag coefficient of $2 \times 10^{-6} \text{ s}^{-1}$. This choice of parameters allows vigorous eddy fields in all simulations. The no-slip boundary condition is an arbitrary choice, and since this may create unrealistic shear near the model boundary, the five nearest grid points to the boundary (25 km) are excluded from the analysis. A time-step of 90 s is chosen as a compromise between model stability and computation time.

The model is forced by the wind stress shown in Figure 1. In the circular domain the stress is purely azimuthal and given by

$$\tau^\theta(r) = a \frac{r}{4} (2 - b^2 r^2), \quad (5)$$

where a is chosen such that the maximum anti-cyclonic wind stress curl is equal to 0.02 N m^{-2} , and $b = 1/R$. This profile is similar to that used in Davis et al. (2014) but avoids very large wind stress at the center of the gyre. The wind stress curl,

$$\nabla \times \tau = \frac{1}{r} \left[\frac{\partial(r\tau^\theta)}{\partial r} \right] = a(1 - b^2 r^2), \quad (6)$$

ramps down quadratically from the maximum at the gyre center to zero at the boundary of the circular basin. Outside the circular basin, the stress (in Cartesian directions) is given by

$$\tau^x = C \left(\frac{y}{r^2} \right), \quad (7)$$

$$\tau^y = C \left(-\frac{x}{r^2} \right), \quad (8)$$

where C is chosen to match the values at the boundary to the circular basin.

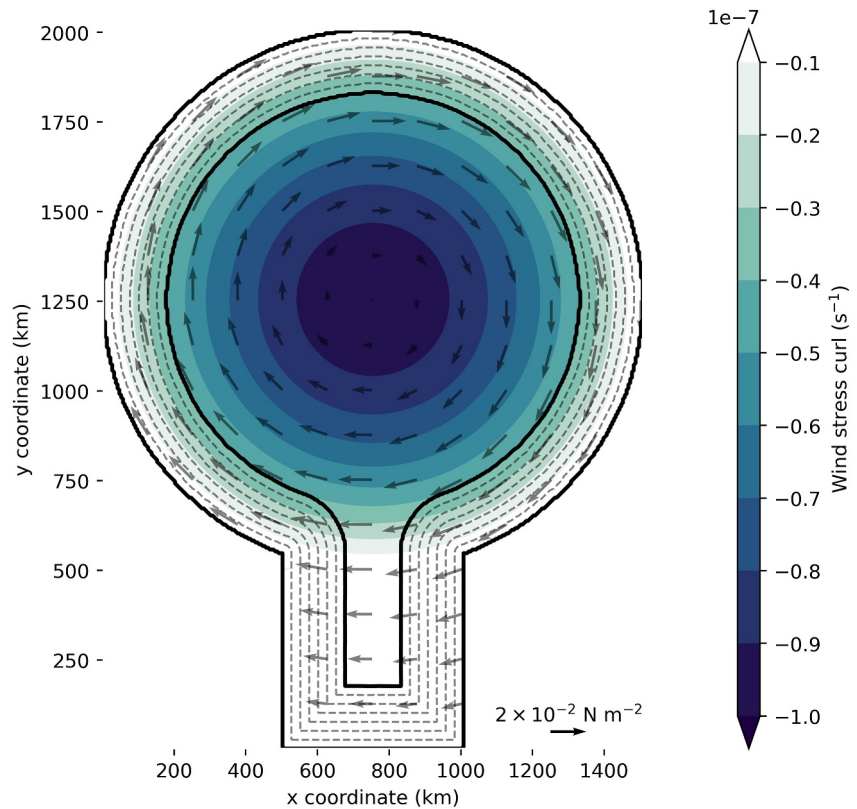


Figure 1. The surface wind forcing of the model. Wind stress is shown as vectors and wind stress curl with shading. Contours of bottom bathymetry are shown in 500 m increments with dashed gray lines, and the solid black line represents the edge of the slope.

The wind stress is ramped up from zero to the maximum over a 20 year period (following a hyperbolic tangent profile) and held like this for another 40 years, forming the spin-up. After these 60 years, there are no long-term trends in kinetic energy and layer volumes, so we consider the simulations to have reached a statistical steady state. The model is then run for an additional 60 years, over which relevant quantities are calculated and stored from 2-day snapshots. A classic time-based Reynold's decomposition is used to define “mean” and “eddy” variables, where the time-mean is taken over the last 60-year simulation period.

There are four distinct runs, each having a different continental slope width—corresponding to slope steepness of 1.5%, 2%, 4%, and 6%. One additional simulation with vertical sidewalls is also run, although this is not studied in detail.

2.2. Linear Stability Calculations

Since our idealized Beaufort Gyre is circular, the linear stability of the flow is evaluated in a 3-layer stacked shallow-water model cast in cylindrical coordinates $(r, \theta, j \in \{1, 2, 3\})$. For each layer we use the two inviscid momentum equations and the adiabatic layer thickness equation:

$$\frac{\partial u_j}{\partial t} + u_j \frac{\partial u_j}{\partial r} + \frac{v_j}{r} \frac{\partial u_j}{\partial \theta} - \frac{v_j^2}{r} - f v_j = -\frac{\partial \phi_j}{\partial r}, \quad (9)$$

$$\frac{\partial v_j}{\partial t} + u_j \frac{\partial v_j}{\partial r} + \frac{v_j}{r} \frac{\partial v_j}{\partial \theta} + \frac{u_j v_j}{r} + f u_j = -\frac{1}{r} \frac{\partial \phi_j}{\partial \theta}, \quad (10)$$

$$\frac{\partial h_j}{\partial t} = -\frac{1}{r} \frac{\partial (r u_j h_j)}{\partial r} - \frac{1}{r} \frac{\partial (v_j h_j)}{\partial \theta}. \quad (11)$$

Here u and v are the radial and azimuthal velocity components, respectively, ϕ is the kinematic pressure and h is the layer thickness. The pressures in the three layers are given by:

$$\phi_1 = g\eta, \quad (12)$$

$$\phi_2 = g\eta + g'_{12}\eta_{12}, \quad (13)$$

$$\phi_3 = g\eta + g'_{12}\eta_{12} + g'_{23}\eta_{23}, \quad (14)$$

where η is the sea surface displacement and η_{12} and η_{23} are the displacements of interfaces (isopycnals) between layers 1 and 2 and layers 2 and 3, respectively. Finally, g is the gravitational acceleration while g'_{12} and g'_{23} are the two reduced gravities (defined in Section 2.1). The total layer thicknesses become

$$h_1 = H_1 + \eta(r, \theta, t) - \eta_{12}(r, \theta, t), \quad (15)$$

$$h_2 = H_2 + \eta_{12}(r, \theta, t) - \eta_{23}(r, \theta, t), \quad (16)$$

$$h_3 = H_3(r) + \eta_{23}(r, \theta, t), \quad (17)$$

where H_1 , H_2 , and H_3 are layer thicknesses in the absence of motion. Note that H_3 can vary in the radial direction to account for the bottom slope (but for these stability calculations we omit the small-scale noise in the topography; see Section 2.1). With these definitions, the actual depth of the two interfaces become

$$z_{12} = -H_1 + \eta_{12}, \quad (18)$$

$$z_{23} = -(H_1 + H_2) + \eta_{23}. \quad (19)$$

We now linearize around an azimuthal and time-mean azimuthal flow \bar{v}_j which is assumed to be in geostrophic balance with the azimuthal and time-mean pressure field. So, for each layer, we write

$$u = u'(r, \theta, t), \quad (20)$$

$$v = \bar{v}(r) + v'(r, \theta, t), \quad (21)$$

$$[\phi, h, \eta] = [\bar{\phi}, \bar{h}, \bar{\eta}](r) + [\phi', h', \eta'](r, \theta, t), \quad (22)$$

where bars and primes indicate the background state and perturbations, respectively. The geostrophic background flow in layer j is given by

$$f\bar{v}_j = \frac{\partial \bar{\phi}_j}{\partial r} \quad (23)$$

and the linearized equations for the perturbations in the same layer (assumed to be much smaller than the background mean variables) take the form

$$\frac{\partial u'_j}{\partial t} + \frac{\bar{v}_j}{r} \frac{\partial u'_j}{\partial \theta} - \frac{\bar{v}_j}{r} v'_j - f v'_j = -\frac{\partial \phi'_j}{\partial r}, \quad (24)$$

$$\frac{\partial v'_j}{\partial t} + u'_j \frac{\partial \bar{v}_j}{\partial r} + \frac{\bar{v}_j}{r} \frac{\partial v'_j}{\partial \theta} + \frac{\bar{v}_j}{r} u'_j + f u'_j = -\frac{1}{r} \frac{\partial \phi'_j}{\partial \theta}, \quad (25)$$

$$\frac{\partial h'_j}{\partial t} = -\frac{\partial(u'_j \bar{h}_j)}{\partial r} - \frac{\bar{h}_j}{r} u'_j - \frac{\bar{h}_j}{r} \frac{\partial v'_j}{\partial \theta} - \frac{\bar{v}_j}{r} \frac{\partial h'_j}{\partial \theta}. \quad (26)$$

The final step is to assume a wave solution in the azimuthal direction for all perturbations,

$$\left[u'_j, v'_j, \phi', h'_j \right] (r, \theta, t) = \text{Re} \{ [u_j, v_j, \phi, h_j] (r) e^{i(l\theta - \omega t)} \}, \quad (27)$$

where the azimuthal wavenumber l is an integer larger than zero. Inserting into Equations 24–26 gives the algebraic equation set

$$-i\omega u_j + il \frac{\bar{v}_j}{r} u_j - \frac{\bar{v}_j}{r} v_j - f v_j = -\frac{\partial \phi_j}{\partial r}, \quad (28)$$

$$-i\omega v_j + u'_j \frac{\partial \bar{v}_j}{\partial r} + il \frac{\bar{v}_j}{r} v_j + \frac{\bar{v}_j}{r} u_j + f u_j = -il \frac{1}{r} \phi_j, \quad (29)$$

$$-i\omega h_j = -\frac{\partial (u'_j \bar{h}_j)}{\partial r} - \frac{\bar{h}_j}{r} u'_j - il \frac{\bar{h}_j}{r} v'_j - il \frac{\bar{v}_j}{r} h_j. \quad (30)$$

In practice, we write the pressure and thickness perturbations in terms of sea surface and interface displacements, using Equations 13 and 16, so that the equation set is in terms of u , v , and η . The equations for each layer are then discretized on a staggered grid in the radial direction, with v and η variables on the same points and u variables half-way between these. After applying the kinematic lateral boundary conditions $u = 0$ in all three layers at the center of the gyre and at the side walls, (28–30) becomes an eigenvalue problem (for each wavenumber l) for eigenvalues ω and eigenvectors $[u_j, v_j, \eta_j]$.

We thus interpolate the time-averaged model variables from their native Cartesian grid to a (r, θ) grid, using 3 km resolution in the radial direction to avoid any loss of information. Velocities are also rotated from their original x and y components into radial and azimuthal components. Finally, all fields are averaged azimuthally. Since the radius of our gyre is 750 km and the radial grid spacing is 3 km, we get 250 v/η -points and 249 u -points. Thus, for three layers, we get a 2247×2247 eigenvalue problem which is solved using the `eig` function in Matlab. The imaginary part of eigenvalue ω gives the growth rate of any given mode, and we keep and study the fastest-growing modes for analysis.

3. Results

3.1. Finite-Amplitude Fields

3.1.1. Overview

Figure 2 shows a typical snapshot of potential vorticity $PV = (f + \zeta)/h$ (with ζ being relative vorticity) in the upper layer after one of the model runs, “BEAU002”, has spun up. This run, which has a continental slope with steepness 2% (a width of 175 km), will be the primary focus throughout the study. However, all runs contain similar qualitative features as BEAU002, except the one run with vertical side walls. The model flow is turbulent, and the central deep basin in particular is filled with a number of cyclonic vortices that have an equivalent barotropic structure (not shown). The vortex radii here are a few tens of kilometers and thus larger than the internal deformation radius in the central basin. The vortex structure of the flow thus suggests that this region, where there is no ambient PV gradient, is characterized by fully-developed f-plane turbulence. In contrast, the slope region, with its strong topographic PV gradient, hosts a flow field which takes on a mixed wave-turbulence character indicative of weakly unstable and, hence, possibly a marginally critical flow.

The remaining analysis will focus on temporally and azimuthally-averaged fields as a function of radial position. Figure 3 thus shows radial profiles of the background fields from the BEAU002 run. The upper and lower panels of the figure show the shape of the two isopycnals and the layer azimuthal velocities, respectively. The upper panel also shows the wind stress and the bottom topography profiles. As in all other figures that will follow, we show the fields from 175 km and outward since the focus is on the dynamics in the vicinity and over the continental slope. The outer 25 km are also omitted from the plots since the upper part of the slope is likely impacted by wall effects, for example, the no-slip lateral boundary condition.

We observe the expected depression of isopycnals toward the center of the basin and anti-cyclonic flow in all layers, with a progressively weaker flow at depth. It is worth comparing the details of the radial flow profiles with what

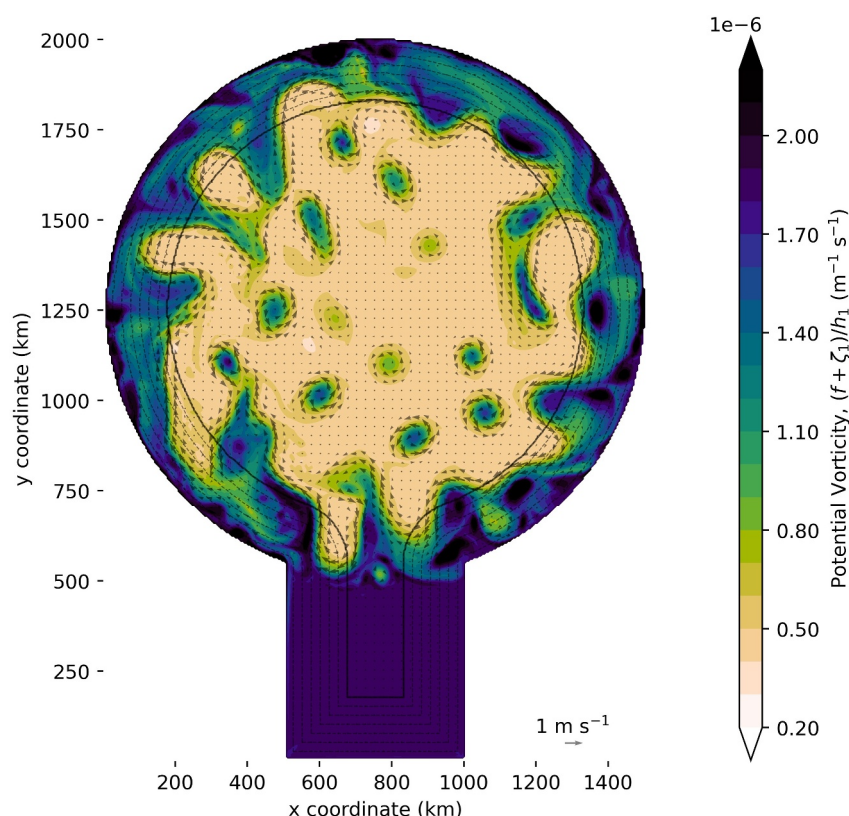


Figure 2. Snapshot of potential vorticity in the upper layer of simulation BEAU002 after spin-up. Arrows represent the instantaneous velocity in the upper layer, and the solid black line represents the lower edge of the continental slope.

would be expected from a linear model of periodic flows around closed ambient PV contours (e.g., Nøst & Isachsen, 2003). In the absence of lateral momentum fluxes, the bottom stress would have to balance the wind stress at each radial position. So the flow strength, at least in the bottom layer, would closely track the wind strength. In a stratified fluid, such transfer of wind momentum to the bottom layer would be mediated primarily by eddy form stresses, as small-scale turbulent stresses are assumed to be negligible away from the top and bottom boundary layers (see e.g. WS18). Figure 3 reveals a much more complex flow profile. The lower layer has a distinct flow maximum—a jet—located over the deep flat basin, far offshore from the wind stress maximum which is over the continental slope (at radial position 612 km). In fact, over the continental slope itself the flow in the lower layer drops to near zero. Apparently, the vertical transfer of momentum to this layer all but vanishes there. This contrasts with the situation in the flat-bottom simulation that has vertical side walls (not shown). There the lower layer flow maximum coincides nearly perfectly with the wind stress maximum, as would be expected if eddy form stress is able to connect the top and bottom frictional layers so that lateral momentum fluxes become unimportant.

The flow profiles in the upper two layers also only mimic the wind profile in a very broad sense. Here too there is a jet, most visible in the top layer, which is clearly offset from the wind stress maximum. As shown in Figure 4, in all simulations the mean-flow maxima do not track the wind maximum but rather the configuration of the continental slope. Specifically, the upper layer jet is centered over the lower break of the continental slope while the lower layer maximum is always located slightly seaward of this position. This behavior is in agreement with the flows observed in the primitive equation simulations of both WS18 and MI19, but here we show that this is a robust feature over a range of bottom slopes.

To start examining what lies behind the uneven velocity profiles, the lateral eddy momentum flux $\overline{u'v'}$ in the three layers are shown in Figure 5. As for all analyses in this study (as outlined in Section 2.2), the calculation has been done in cylindrical coordinates where r and θ are the radial coordinate and azimuthal angle, respectively, and u and v are the corresponding velocity components. Furthermore, the overline in the expression indicates a combined azimuthal and temporal mean, while the primes indicate deviations from such means. A positive value of

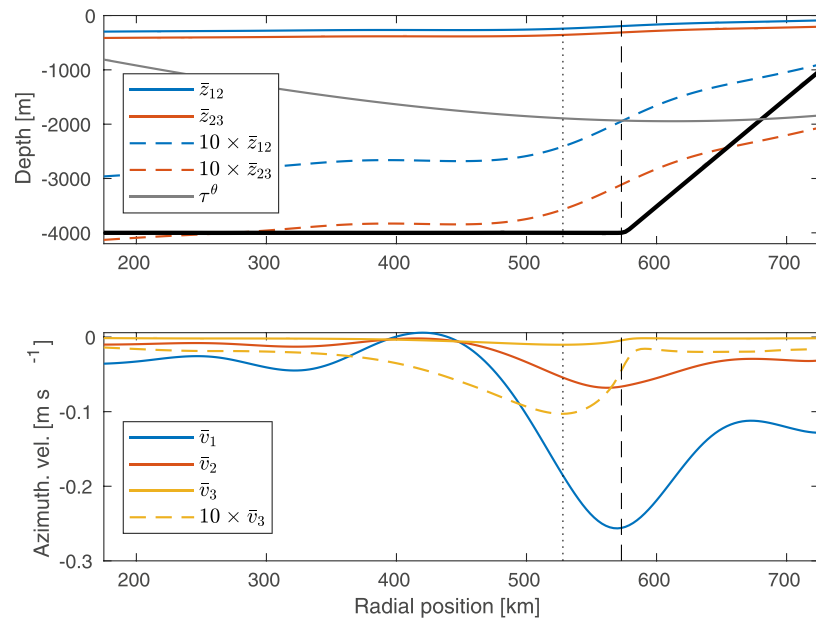


Figure 3. Temporally and azimuthally-averaged fields from the BEAU002 simulation (having a bottom slope of 2%). The top panel shows the depth of the isopycnals between layers 1 and 2 (\bar{z}_{12} ; blue) and layers 2 and 3 (\bar{z}_{23} ; red). Solid lines give the actual depth while dashed lines show depths multiplied by a factor 10. Shown are also the wind stress profile (τ^θ ; gray line, arbitrary units) and the bottom topography (thick black line). The bottom panel shows the azimuthal velocity profiles \bar{v} for the top (blue), middle (red) and bottom (yellow) layers. The flow in the bottom layer is also shown after multiplication by a factor 10 (dashed yellow line). In both panels vertical black lines indicate the position of the slope break (dashed) and the velocity maximum in the lower layer (dotted). Note that the inner 375 km and outer 25 km of the domain have been excluded from this and subsequent profile plots.

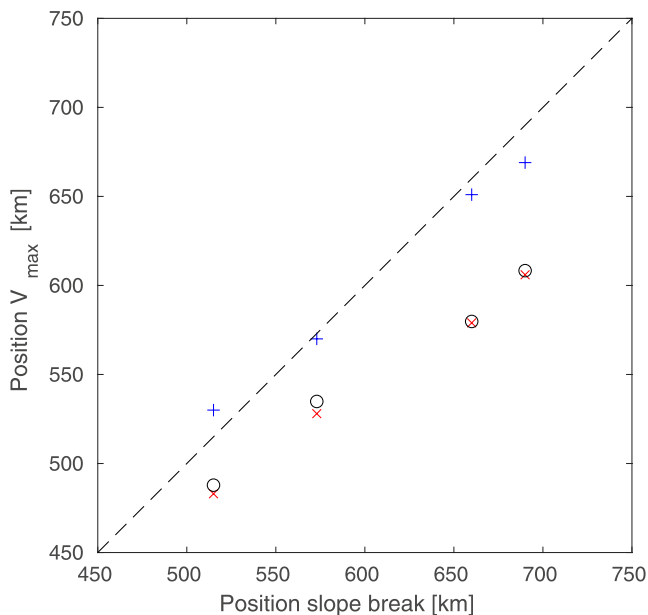


Figure 4. The positions of the velocity maximum in the top layer (blue crosses) and in the lower layer (red x's) as a function of the position of the bottom of the continental slope. Also shown are the positions of the peak in the top layer eddy form drag (black circles).

$\overline{u'v'}$ indicates a shoreward eddy flux of cyclonic momentum or, alternatively, a seaward flux of anti-cyclonic momentum. We see that in the directly-forced top layer, eddies transfer anti-cyclonic momentum seaward over and around the continental slope. There is an onshore flux of anti-cyclonic momentum in the deep basin, but this is very weak. Finally, there is also a weak offshore flux in the middle layer but not in the lower layer.

Are these momentum fluxes the result of barotropic instability in the upper two layers? To assess this, we can form evolution equations for eddy kinetic energy (EKE) by multiplying the linearized momentum equations (Equations 9 and 10) by u' and v' , respectively, adding the two expressions and finally integrating over the mean layer thickness (see e.g. Ghaffari et al., 2018). The resulting EKE evolution equation then contains a “barotropic conversion” term between mean and eddy kinetic energy:

$$C_{bt} = -\overline{hu'v'} \frac{\partial \bar{v}}{\partial r}. \quad (31)$$

A positive C_{bt} value indicates that azimuthal momentum is fluxed out of the mean flow, thus broadening any existing current and reducing mean-flow KE—the classic signature of barotropic instability (e.g., G. K. Vallis, 2017). However, the diagnostics done here, also shown in Figure 5, indicate a somewhat more complex picture, with momentum fluxed into the mean upper layer jet over the continental slope and out of the jet seaward of the slope. Eddies are therefore sharpening the jet, that is, forming it, over the continental slope, and then broadening it over the flat regions further offshore.

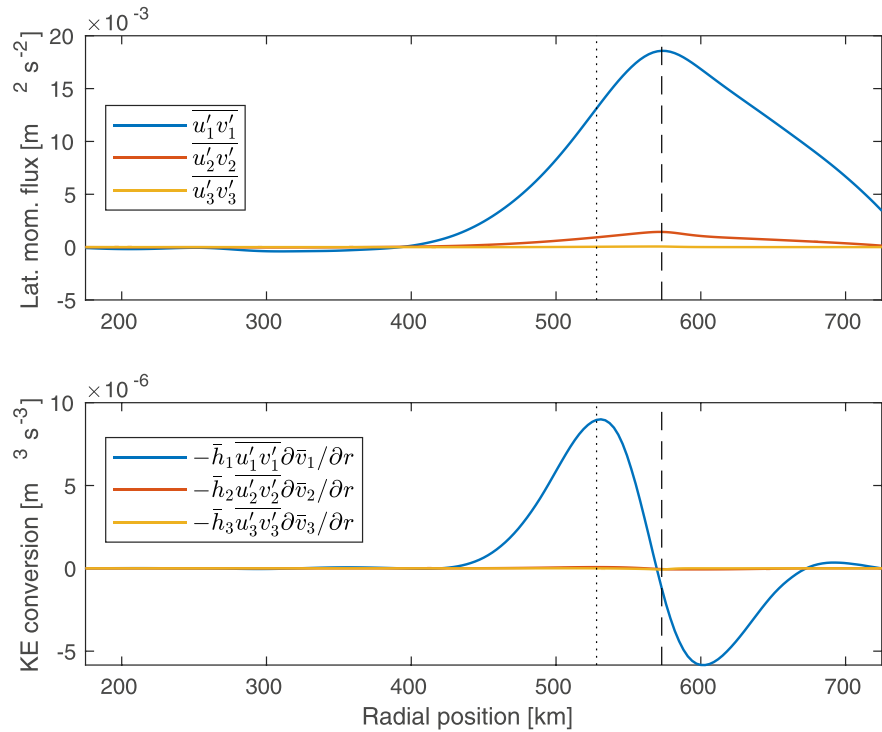


Figure 5. Upper panel: lateral eddy momentum fluxes $\overline{u'v'}$ for the BEAU002 simulation. Lower panel: the corresponding barotropic energy conversion term $-\overline{h u'v'} \partial \bar{v} / \partial r$. The solid lines indicate upper layer (blue), middle layer (red) and lower layer (yellow). The vertically dashed and dotted lines indicate the positions of the slope break and lower layer velocity maximum, respectively.

How this behavior relates to the linear stability of the flow will be examined in the next section. But first, we continue to examine how eddy momentum fluxes, in a broader sense, relate to the observed mean flow. These fluxes redistribute the azimuthal wind stress around in the system, between layers and within each layer, and the flow can be expected to be accelerated where there is a convergence of such fluxes. The lateral convergence, that is, $-\partial \overline{u'v'} / \partial r$, can be deduced from the slope of the flux curve in the top panel of Figure 5. This shows that the maximum lateral convergence of anti-cyclonic momentum flux in the top two layers, that is, the inflection point in the flux curve, takes place directly over the lower layer velocity maximum. It therefore appears that eddy fluxes may be driving the lower layer, but a more comprehensive picture will require actual diagnostics of vertical eddy momentum fluxes.

3.1.2. PV Fluxes

The net impact of combined lateral and vertical eddy momentum fluxes can be captured in a thickness-weighted average of the azimuthal momentum equation. An approximate Transformed Eulerian Mean (TEM) expression for a given layer, in polar coordinates and assuming QG scaling for the eddy motions, is (for a derivation in Cartesian coordinates, see G. K. Vallis, 2017, chapter 10):

$$\frac{\partial \bar{v}}{\partial t} + f \bar{u}^* = -\frac{1}{r} \frac{\partial}{\partial r} \left(r \overline{u'v'} \right) + \frac{1}{h} \left(\overline{\phi' \frac{1}{r} \frac{\partial \eta'_t}{\partial \theta}} - \overline{\phi' \frac{1}{r} \frac{\partial \eta'_b}{\partial \theta}} \right) + \frac{\bar{\tau}_t^\theta}{h} - \frac{\bar{\tau}_b^\theta}{h}, \quad (32)$$

where the overbar now only indicates an azimuthal average. Here η_t and η_b are top and bottom interfaces, and τ_t^θ and τ_b^θ represent small-scale turbulent vertical momentum fluxes through those interfaces (turbulent stresses). Note that \bar{u}^* in the Coriolis term is the time-varying residual radial velocity of the layer,

$$\bar{u}^* = \bar{u} + \frac{\overline{u' h'}}{\bar{h}}, \quad (33)$$

that is, the effective mass transport velocity. So the lateral (radial) convergence of azimuthal momentum fluxes, in combination with a vertical convergence of interfacial form stress and/or turbulent stress, can accelerate the flow in the layer. Just like turbulent stresses $\bar{\tau}^\theta$, the form stresses $\overline{\phi'(\partial\eta'/r\partial\theta)}$ can be interpreted as vertical (downward) fluxes of azimuthal momentum.

If applying integration by parts around the periodic domain under QG scaling—where (a) azimuthal pressure gradients are linked to radial geostrophic velocities and (b) the lowest-order geostrophic flow is horizontally non-divergent, the form stresses can be rewritten in terms of eddy advection of interface heights and the convergence of the lateral momentum flux can be written in terms of an eddy vorticity flux. The TEM equation can thus be recast as

$$\frac{\partial \bar{v}}{\partial t} + f\bar{u}^* = -\overline{u'\zeta'} + \frac{f}{\bar{h}}(\overline{u'\eta'_t} - \overline{u'\eta'_b}) + \frac{\bar{\tau}_t^\theta}{\bar{h}} - \frac{\bar{\tau}_b^\theta}{\bar{h}}, \quad (34)$$

where ζ is relative vorticity. Finally, since $\eta'_t - \eta'_b = h'$, we arrive at the final expression

$$\frac{\partial \bar{v}}{\partial t} + f\bar{u}^* = -\overline{u'q'} + \frac{\bar{\tau}_t^\theta}{\bar{h}} - \frac{\bar{\tau}_b^\theta}{\bar{h}}, \quad (35)$$

where $\overline{u'q'}$ is the QG PV flux,

$$\overline{u'q'} = \overline{u'\zeta'} - \frac{f}{\bar{h}}\overline{u'h'}, \quad (36)$$

that is, the QG approximation of the total eddy PV flux. The eddy forcing of the azimuthal mean flow of any given layer therefore consists of a lateral vorticity flux and a lateral thickness flux. As seen from Equation 32, the thickness flux can alternatively be interpreted as a form drag on the layer, and below we will be using these two terms interchangeably.

Figure 6 shows the two contributions, $-\overline{u'\zeta'}$ and $(f/\bar{h})\overline{u'h'}$, to the (negative) PV flux for each of the three layers in the same BEAU002 run. A very robust signal, which is also present in all other runs (not shown), is the reduced eddy form drag (or eddy thickness flux) in the top layer over the continental slope. By inspection of Figure 3, this region has a considerable thermal wind shear. But, apparently, it experiences a much reduced form drag—behavior which is consistent with the suspected suppression of baroclinic instability over a sloping bottom (Blumsack & Gierasch, 1972). The slope region is instead dominated by lateral eddy vorticity fluxes. As pointed out by MI19, these lateral fluxes tend to drive a cyclonic flow over the slope in the top layer or, more appropriately to our configuration here, to counter the anti-cyclonic flow set up by the wind forcing.

The eddy form drag increases in magnitude and dominates seaward of the continental slope, consistent with the notion that baroclinic instability can kick in here, transferring momentum to the layers below. The net effect is observed in Figure 3, that is, a spin-up of the lower layer. In fact, the peak in upper layer eddy form drag coincides almost precisely with the center of the lower layer jet, as can be seen by comparing red crosses and black circles in Figure 4. It is also worth noting that the location of the maximum upper layer form drag corresponds to the largest lateral vorticity flux in the same layer. Eddy vorticity fluxes are therefore forcing the upper layer anti-cyclonically immediately off the continental slope, creating a jet there.

Fluxes in the middle layer are much weaker but, importantly, the eddy vorticity and thickness fluxes consistently oppose one another within this layer, tending to produce a very weak total PV flux. As a result, in this purely wind-driven setting, the middle layer appears to be rather dynamically inactive. In the lower layer, both fluxes all but vanish over the continental slope. The lower layer is therefore practically unforced there, at least by eddy fluxes. However, seaward of the slope the layer experiences a negative form drag, that is, an eddy-mediated

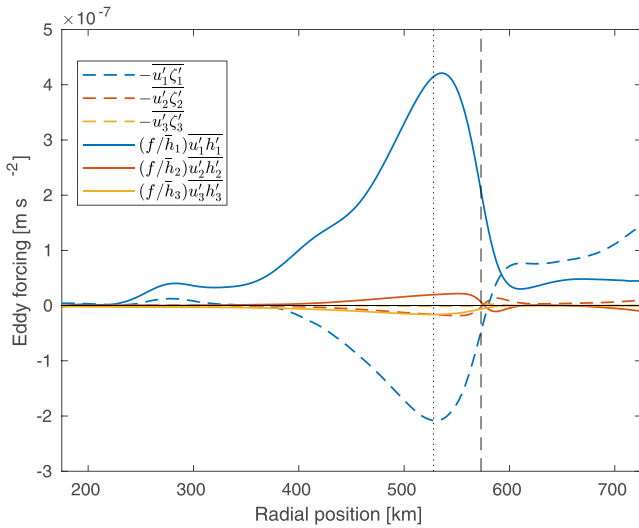


Figure 6. The two components of the negative eddy PV flux (see Equations 35 and 36) in the BEAU002 run: negative vorticity flux $-\overline{u'\zeta'}$ (dashed lines) and lateral thickness flux $(f/\bar{h})\overline{u'h'}$ (solid lines) for each of the three layers (blue = top, red = middle and yellow = bottom). The vertically dashed and dotted lines indicate the positions of the slope break and lower layer velocity maximum, respectively.

transfer of anti-cyclonic momentum from above. So it is here, off the continental slope, that the lower layer can finally be accelerated anti-cyclonically.

Adding the two flux components to form a total QG PV flux (not shown) reveals what can already be deduced from Figure 6, namely that eddy PV fluxes decelerate the wind-driven anti-cyclonic flow in the top layer everywhere. PV fluxes then force the lower layer anti-cyclonically but, importantly, only seaward of the continental slope. Over the slope itself, the lower layer is practically unforced. Finally, the calculation reveals a near-zero eddy forcing of the middle layer everywhere. There are eddy momentum fluxes passing through this layer, but in the equilibrated state these are not convergent.

A PV eddy diffusivity can be estimated in each layer by dividing the QG PV flux by the background PV gradient,

$$\kappa = -\frac{\overline{u'q'}}{\bar{h}\partial\bar{q}/\partial r}, \quad (37)$$

where $\bar{q} = (f + \zeta)/\bar{h}$. For units to match when merging QG and shallow-water formulations, the PV gradient needs to be multiplied by the layer thicknesses. The amplitude will then be off, but our interest here is primarily the sign of the PV gradient and the calculated PV diffusivities. The two quantities are shown in Figure 7. The sign of the background gradient will be examined more closely below, but the figure clearly shows that diffusivities in

all three layers are consistently positive. Since both the PV flux and PV gradient in the middle layer are extremely small everywhere, diffusivities in this layer are somewhat erratic. Upper and lower layer diffusivities however take on quite similar forms, both dropping over the continental slope. But since the PV flux all but vanishes in the lower layer over the continental slope (see Figure 6), the diffusivity there actually tends to zero.

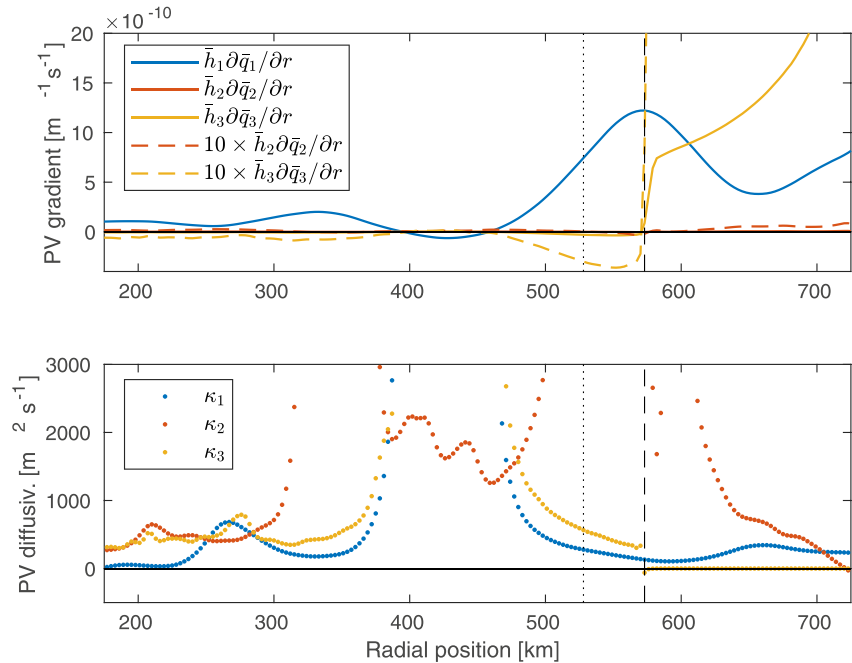


Figure 7. Top panel: the background PV gradient (scaled by layer thickness) in each layer in the BEAU002 run; blue = top, red = middle and yellow = lower layer. Dashed lines show the estimates in the two lower layers multiplied by 10. Lower panel: PV diffusivities from Equation 37 in the three layers. The vertically dashed and dotted lines indicate the positions of the slope break and lower layer velocity maximum, respectively.

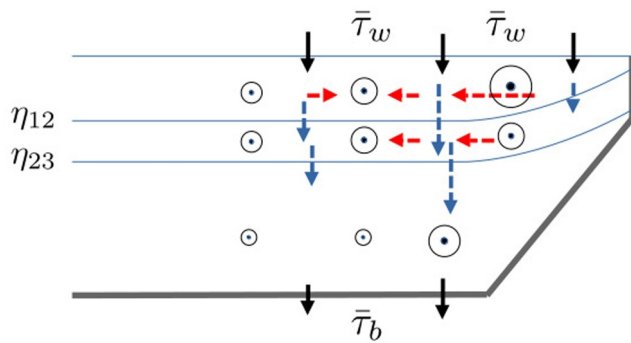


Figure 8. Sketch of wind and eddy fluxes of anticyclonic momentum, as well as the resulting azimuthal mean flow in the three layers. Black arrows show wind and bottom stresses, while red and blue dashed arrows show eddy lateral momentum fluxes and form stresses, respectively.

The key dynamics observed above are sketched in Figure 8 (see also Figure 2 of Wang & Stewart, 2018). In summary, eddy form stress, that is, the vertical transfer of wind momentum from the upper to deeper layers, is severely hampered by the topographic PV gradient over the continental slope. However, nature still finds a way, by transporting the wind momentum offshore, just off the continental slope, where it can be efficiently transferred to lower layers—and ultimately into the ground. The lateral eddy fluxes in upper layers are thus a direct consequence of the suppression of vertical momentum flux over the continental slope. Finally, the dynamics as a whole appear to be related to down-gradient PV fluxes, except for in the lower layer where they vanish.

3.2. The Linear Stability of the Mean Flow

3.2.1. Integral Constraints and Growth Rates

We now consider the stability properties of the background flow and ask whether unstable modes from a linear stability calculation (Section 2.2) can

explain at least some of the finite-amplitude fluxes seen above. As discussed in the Introduction, that they should do so is not obvious, given the possibility that nonlinear eddy-eddy interactions can produce for example, an inverse energy cascade that will bring eddy characteristics away from the linear prediction. However, as shown in Figure 2, whereas the flat central basin is dominated by coherent vortices (a sign of strongly nonlinear eddy-eddy interactions), the region over and just offshore of the continental slope is characterized by a mixed turbulence-wave structure—suggesting weakly nonlinear conditions over our primary region of interest.

Additional suggestion that the flow over the slope is near marginal criticality can be drawn from Figure 3, which shows that the steep continental slope hinders a reversal of the thickness PV gradient over the slope itself—much like it does in the real Beaufort Gyre (see e.g. Fig. 1 in MI19 and the discussion above). The Phillips-type criticality measure (Equation 3) thus suggests subcritical conditions here, but that classical measure neglects relative vorticity contributions to the PV. It is therefore worth looking again at the full background PV gradient plotted in the upper panel of Figure 7. To repeat, the Charney-Stern-Pedlosky integral constraint states that a necessary condition for instability is that the lateral PV gradient changes sign somewhere in the domain (see e.g. G. K. Vallis, 2017).

Figure 7 shows that the total PV gradient—now also accounting for relative vorticity gradients—does not change sign in the vertical, that is, between layers, over the continental slope. This is consistent with the prediction of the modified Eady model of Blumsack and Gierasch (1972), that very steep retrograde bottom slopes can stabilize the flow. The gradient in the top layer alone also does not change sign laterally until quite far off the slope, and in other simulations the gradient keeps one-signed across the entire domain (not shown). The lateral momentum fluxes observed over the slope in the top layer are therefore likely not tied to pure barotropic instability. This also appears to be in agreement with the observations that momentum fluxes over the slope region are both up and down the background velocity gradient. The most striking PV gradient sign change takes place in the lower layer, right at the bottom of the slope where the topographic PV gradient vanishes. Velocities and, especially, lateral eddy momentum fluxes in this lower layer are negligible (Figure 5), so the sign change does not suggest lateral shear instability in that layer. However, the removal of the topographic PV gradient in the lower layer has now caused a sign reversal in the vertical direction, between the upper and lower layer. Thus, the classical integral constraint for baroclinic instability is fulfilled and, as such, makes qualitative sense of the strong eddy form stresses seen right off the slope in Figure 6. And yet, lateral momentum fluxes in the upper layer connect the seemingly baroclinically stable slope region to the unstable flat region immediately offshore. We therefore continue with linear stability calculations to investigate if this fairly complex flux pattern can be found in any of the unstable modes.

As in the above, the focus will be on the BEAU002 run. Using temporally and azimuthally-averaged fields from this simulation, the eigenvalue problem is solved for a set of integer azimuthal wavenumbers from 1 to 40 (wavenumber 1 corresponds to one wavelength spanning the circumference of the basin, etc.). For each wavenumber, the six fastest-growing unstable modes were then recorded, and the growth rates for these modes are plotted in Figure 9. There is some overlap between unstable modes, but we have highlighted a few distinguishable “lobes” of unstable growth that individually extend across a range of wavenumbers. One such lobe stands out,

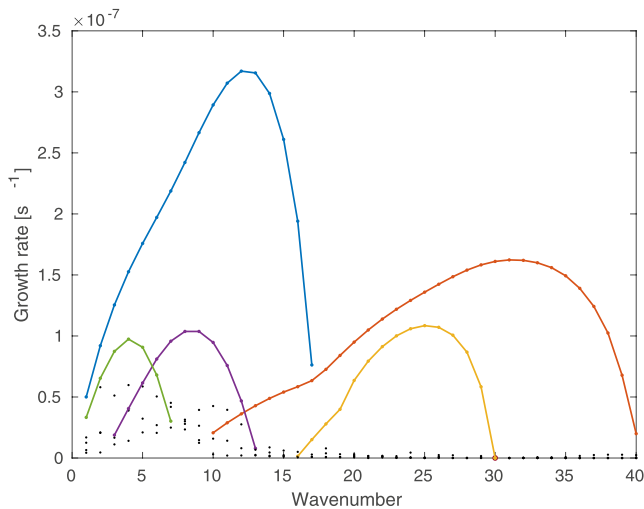


Figure 9. The growth rates of the six fastest-growing unstable modes at each wavenumber in the BEAU002 simulation. A few distinguishable lobes of unstable growth are highlighted with colored lines.

producing the absolute fastest growth at $l = 12$. As will be seen below, this lobe likely contributes significantly to the observed PV fluxes over the slope region.

3.2.2. The Fastest-Growing Mode

Figure 2 suggests the presence of an azimuthal mode 12–13 weakly-nonlinear wave along the lower parts of the continental slope. We take this as indication that characteristics of the fastest-growing linear mode, the one at $l = 12$, are indeed intact at finite amplitude. It therefore seems warranted to investigate whether the eddy fluxes predicted by this mode, assembled from its eigenvector that consist of perturbation velocities and interface heights (see Section 2.2), can explain some of the finite-amplitude fluxes seen above.

The thickness and vorticity fluxes of the $l = 12$ mode are shown in Figure 10. Although absolute magnitudes are arbitrary (the eigenvector of each mode has norm one), the horizontal structures may be compared with their finite-amplitude counterparts shown in Figure 6. There are clear discrepancies, perhaps most strikingly observed over the central deep basin. Whereas the finite-amplitude PV fluxes extend almost throughout the entire basin, the linear mode produces fluxes that only reach about 150 km seaward of the

continental slope. However, the linear mode captures what is arguably the key signal seen in these simulations, as well as in the primitive equation simulations of WS18 and MI19: namely suppressed eddy form stresses over the continental slope and, instead, a lateral transfer of upper-layer momentum off the slope. There, off the slope, form stresses in the linear mode transfer wind momentum to the lower layer, nearly precisely where the lower layer velocity maximum is observed—just as seen in the finite-amplitude fields. The linear mode also qualitatively captures some key features in the lower layer, including form drag forcing of this layer very near its observed velocity maximum. Finally, the eigenvectors of the mode also produce a near perfect cancellation between thickness and vorticity fluxes in the middle layer, reflecting the near-zero PV gradient in that layer.

This fastest-growing linear mode at wavenumber $l = 12$ therefore contains several of the essential characteristics of the finite-amplitude eddy fluxes around the continental slope. However, as noted above, the mode fails at explaining eddy form stresses far off the continental slope in the deep basin. That there is an active form stress over the entire deep basin is consistent with sustained sign reversals of the PV gradient between the upper and lower layers there (as can be clearly seen from Figure 7). But these fluxes are not associated with the fastest-growing $l = 12$ mode. Finally, there are also discrepancies over the upper parts of the continental slope.

Whereas the linear mode has an upper-layer form stress that monotonically tends to zero over the slope—in agreement with the suggested impact of the topographic PV gradient—the finite-amplitude form stress, while considerably suppressed, stays finite over the entire slope region. A similar discrepancy is seen in vorticity fluxes, where the linear mode suggests a gradual fall-off while finite-amplitude fluxes actually rise somewhat over upper parts of the slope.

3.2.3. Other Unstable Modes

Do other unstable modes contribute to the observed finite-amplitude fluxes, particularly over the upper parts of the continental slope and over the deep basin? Some indication can be had from Figures 11 and 12, which show thickness fluxes and vorticity fluxes in the top layer for the two fastest-growing linear modes at each wavenumber. Here, the estimates have been scaled by the growth rate for each mode. The resulting values (colors in the figure) can not be taken as indication of the exact level at which each mode would equilibrate if allowed to grow to finite amplitude, but scaling by the growth rate should nevertheless give some indication of the relative importance of the various modes.

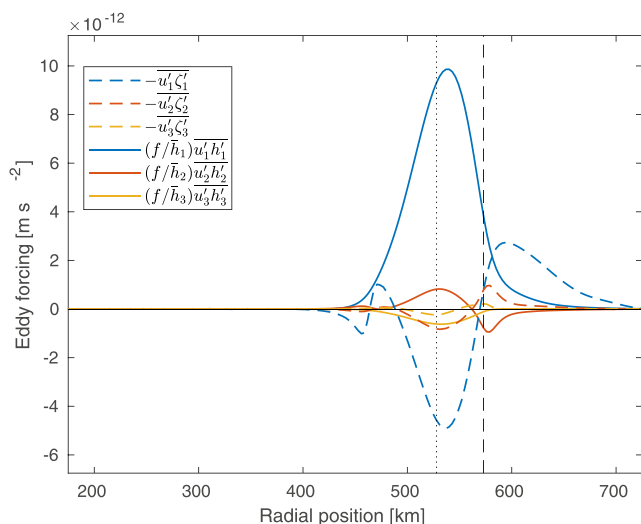


Figure 10. Same as Figure 6 but now calculated from the eigenvector of the fastest-growing unstable linear mode at wavenumber $l = 12$.

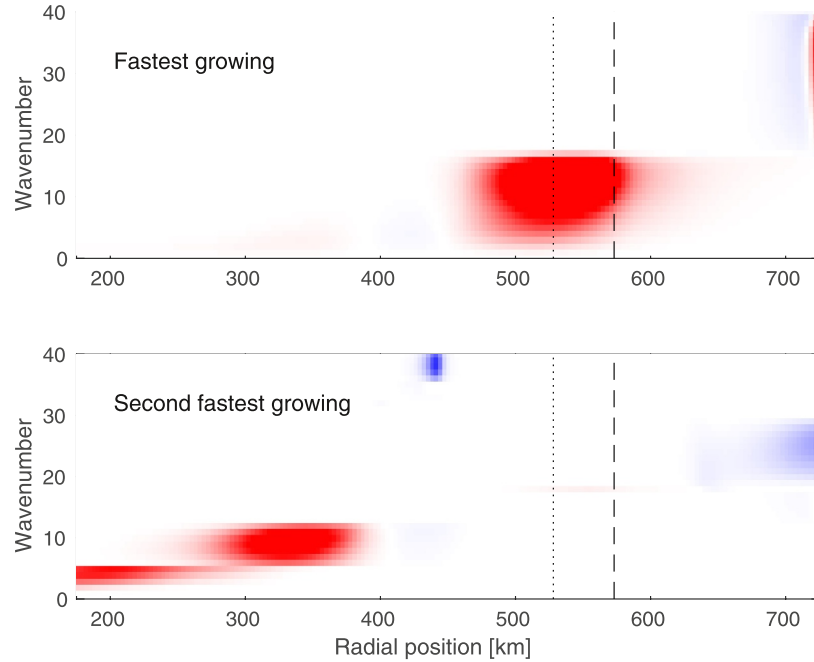


Figure 11. Lateral thickness fluxes $(f/\bar{h})\overline{u'h'}$ in the upper layer calculated from the eigenvectors of the linear stability calculations, for mode 1 (fastest-growing; upper panel) and mode 2 (second fastest-growing; lower panel). Magnitudes are arbitrary, but red and blue colors signify positive and values, respectively. The vertically dashed and dotted lines indicate the positions of the slope break and lower layer velocity maximum, respectively.

As was already evident from Figure 9, the fastest-growing mode at $l = 12$ is part of a dynamical feature, a “lobe,” which is unstable across a range of wavenumbers. Figures 11 and 12 suggest that this main lobe dominates both thickness and relative vorticity fluxes over the lower parts and immediately offshore of the slope. It is also

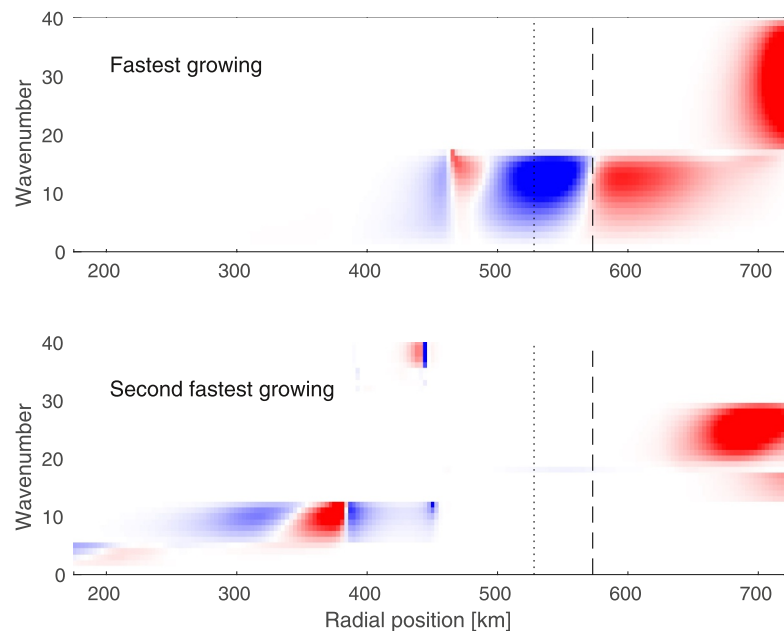


Figure 12. Same as in Figure 11 but for lateral vorticity fluxes $-\overline{u'\zeta'}$.

responsible for part of the vorticity flux over the slope itself, particularly over the lower part. However, as already seen above, the lateral vorticity flux of this lobe falls to zero over the upper parts of the slope. There, two other lobes which dominate unstable growth $l > 20$ take over to dominate the vorticity flux.

Neither of these dominant lobes of unstable growth contribute to form stresses and vorticity fluxes over the deep and flat basin. But other modes contribute here, apparently growing due to the sign reversal of the PV gradient between the top and bottom layer. The one feature of finite-amplitude fluxes that we see no trace of from the linear calculations is a finite eddy form stress, or thickness flux, in the upper layer over the upper parts of the continental slope. Here all linear modes contain near-vanishing fluxes, or even, as seen from the second-fastest-growing mode in Figure 11, reversed fluxes. This important feature of the slope dynamics thus appears to be a truly finite-amplitude non-linear effect.

4. Discussion and Conclusions

Much of the dynamical behavior observed in this study can be seen as confirmation of the results presented by WS18 and MI19. However, by idealizing the model further, to three isopycnal layers only, we have been able to extract somewhat cleaner signals. Perhaps the biggest advantage of the present 3-layer formulation is the ease with which one can investigate the linear stability properties of the background flow in a 2D framework. The very obvious role of lateral momentum fluxes seen in these model runs, as well as in the simulations of WS18 and MI19, points to the need for such 2D analysis. The classical 1D QG stability analysis conducted by WS18 is unable to pick up the dynamics responsible for the lateral fluxes. Earlier 2D stability analyses have typically used prescribed analytic background fields (e.g., Ghaffari et al., 2018; Lozier & Reed, 2005) and have thus not been able to compare directly with finite-amplitude fluxes. Here, we have seen that some key qualitative features of the observed finite-amplitude PV flux over the continental slope region are reproduced by the fastest-growing unstable mode.

Other unstable modes may also contribute, both over the slope region and in the offshore deep basin. But snapshots of the flow field (e.g., Figure 2) show that the flat deep basin is characterized by coherent vortices that must be indicative of strong eddy-eddy interactions that will not be captured by linear calculations. Nevertheless, the fact that finite-amplitude and linear mode fluxes share key characteristics over and just offshore of the continental slope may be indicative that oceanic flows—if influenced by a strong ambient PV gradient—are also able to adjust themselves into a marginally-unstable state at the wave-turbulence boundary. In these simulations, the classical QG-based criticality parameter measuring the isopycnal slope to bottom slope (Equation 3) suggests that the flow over the slope is subcritical with respect to baroclinic instability. The fact that eddy form stresses there are not identically zero, neither in the linear calculations nor at finite amplitude, could be indication that the classic criticality parameter, being based on the local assumption that lies behind classic QG studies of baroclinic instability (Smith, 2007; Tulloch et al., 2011; Wang & Stewart, 2018), may be an incomplete measure of criticality in a situation with strong lateral velocity shears. But it is also conceivable that some of the non-vanishing finite-amplitude PV fluxes over the upper parts of the continental slope reflect stirring by finite-size eddies generated by instability triggered by PV gradient sign changes at the bottom of the slope.

As seen, even the 3-layer model is unnecessarily complex, as the middle layer in these simulations turned out to be dynamically passive. Indeed, at an earlier stage of this study, separate 2-layer model simulations were run. These actually contained all the key large-scale flow and eddy flux features discussed above. This is in agreement with the arguments that, in a purely wind-driven system, that is, one that experiences barotropic forcing, there is no obvious mechanism which can produce internal PV gradients (Manucharyan & Stewart, 2022). So one may be tempted to conclude that a vertical discretization to two layers is valid for purely wind-driven systems. It is important to remember, however, that the real ocean also experiences buoyancy forcing at the surface where isopycnal layers outcrop, as well as diapycnal mixing in the interior. Both processes can give rise to interior thickness PV gradients that would add to the picture observed in these simulations.

In the real Arctic Ocean, interior layer thickness gradients do exist, as shown by for example, Meneghello et al. (2021, their Fig. 9). That study also suggested that such gradients are dynamically responsible for the presence of sub-surface eddies that act to reduce those very gradients. These eddies have modest vertical and lateral scales, typically a few hundred meters and a few tens of kilometers, respectively. In comparison, the fastest-growing mode $l = 12$ in our set-up will have a half-wavelength of about 135 km around the bottom of the

continental slope ($r = 650$ km). So one is justified in questioning whether these simulations, as well as earlier similar model studies, are of any relevance for the situation in the Beaufort Gyre. It is worth noting, however, that most observations and theoretical studies of such smaller-scale halocline eddies have focused on the central gyre rather than on the continental slope along the rim of the gyre. The possibility also exists that the eddy dynamics are fundamentally different between these two regions. An indication of this may be a notable difference in vertical EKE profiles collected by four long-term moorings in the Beaufort Gyre. As shown in Figure 1 of Manucharyan and Stewart (2022), three moorings that are situated well within the gyre all reveal EKE maxima in the 50–250 m depth range, with rapid fall-off both above and below. In contrast, the last mooring situated over the continental slope off the Chukchi Plateau observed the highest EKE levels at the surface and, importantly, non-negligible energy levels at the bottom. The analysis of Manucharyan and Stewart (2022) does not reveal whether velocity fluctuations in upper and lower layers at this last mooring are correlated, that is, whether the vertical EKE structure reflects a deep unstable mode. If that turns out to be the case, then one can anticipate that the lateral scales are also larger than those of the interior halocline eddies.

There is another peculiarity tied to the large lateral scales obtained in the present stability calculations. In the modified Eady theory of Blumsack and Gierasch (1972), the fastest-growing unstable mode over a retrograde slope has a lateral scale comparable to the internal deformation radius—which is of order 11 km in these simulations. Again, the fastest-growing linear mode found here is much larger than that. But the modified Eady problem does not tackle lateral shears and lateral momentum fluxes. As it turns out, the most unstable mode in our simulations takes on a scale which is approximately that of the width of the lateral shear zone. This, in turn, appears to be set by the width of the continental slope. So it is possible that the internal deformation radius is no longer the most relevant length scale for the problem at hand—and neither along the Beaufort Gyre continental slope.

An interesting signal obtained in this layer model is the consistently down-gradient PV flux. The flux is able to homogenize PV nearly in the middle layer. But just as important to our dynamical understanding is the vanishing PV flux and diffusivity in the lower layer over the continental slope. So the lower layer is not forced over the slope and, as seen in Figure 3, has near-zero flow there. This last result is in slight disagreement with WS18 and MI19 who found weak but non-zero prograde currents over the lower parts of their continental slope. Eddy-driven prograde flows, bottom-trapped in stratified systems, are predicted by both minimum potential enstrophy and maximum entropy arguments (Bretherton & Haidvogel, 1976; Salmon et al., 1976; Venaille, 2012). We are unable to explain why prograde flows do not arise in the 3-layer simulations here, but note that such eddy-induced prograde flows—here in the opposite direction to the wind forcing—imply a local raising of APE near the bottom and thus depend on the energetics of the eddy field.

The most significant limitation of the study, in addition to the model's low vertical resolution and inability to form small surface-trapped eddies, may be its neglect of irregular bottom variations, like corrugations and canyons. The possible excitation of standing topographic waves under the retrograde conditions we are studying here may give rise to additional form stresses that impact both buoyancy and momentum budgets to lowest order, as indicated by for example, Wang and Stewart (2020). Bottom corrugations can also add form stress for prograde flows, but this does not involve energy accumulation into standing waves and thus appears to be of much lower importance (Bai et al., 2021). Given that the Arctic Ocean's Beaufort Gyre is in fact retrograde, further investigation into this issue seems warranted.

If lateral momentum fluxes are still important, even if form stresses from standing waves are acting, then any topographically-aware mesoscale eddy parameterization for use in coarse-grained climate models needs to account for this. The results obtained here should be a reminder that a successful formulation needs to (a) include lateral momentum fluxes and (b) be constrained to ensure down-gradient transport of full PV throughout the water column. Additionally, in the situation studied here with smooth topography, the parameterized PV flux near the bottom should vanish over steep retrograde topography, a result which is also predicted by the modified Eady model of Blumsack and Gierasch (1972). However, again, more work needs to be done in the situation where bottom corrugations are present—as they obviously are in the real ocean. Early assessments by Wang and Stewart (2020) suggest that standing waves contribute, but that eddy form stress is still reduced over retrograde slopes. This should not come as a surprise; any exchanges of semi-rigid water columns across sloping topography—the rigidity stemming from Earth's rotation—should be hampered.

Data Availability Statement

The isopycnal model used in this manuscript, Aronnax, is archived in a Zenodo repository (Doddridge & Radul, 2018). The code used to configure Aronnax for the experiments described in this manuscript and resulting model configuration files, the processed model output, and code used to carry out linear stability analysis, are archived in a separate Zenodo repository (Isachsen et al., 2023).

Acknowledgments

This study was part of the TopArctic project funded by the Norwegian Research Council (Grant 314826). We would like to thank Ed Doddridge for leading the development of Aronnax, and his support in designing and running earlier versions of the simulations described in this study. Finally, we also thank Francis Poulin, an anonymous reviewer and the associate editor of the journal for very useful comments on the manuscript.

References

- Bai, Y., Wang, Y., & Stewart, A. L. (2021). Does topographic form stress impede prograde ocean currents? *Journal of Physical Oceanography*, 51, 2617–2638. <https://doi.org/10.1175/JPO-D-20-0189.1>
- Blumsack, S. L., & Gierasch, P. J. (1972). Mars: The effects of topography on baroclinic instability. *Journal of the Atmospheric Sciences*, 29(6), 1081–1089. [https://doi.org/10.1175/1520-0469\(1972\)029<1081:mteoto>2.0.co;2](https://doi.org/10.1175/1520-0469(1972)029<1081:mteoto>2.0.co;2)
- Bretherton, F., & Haidvogel, D. (1976). Two-dimensional turbulence over topography. *Journal of Fluid Mechanics*, 78(1), 129–154. <https://doi.org/10.1017/s002211207600236x>
- Cushman-Roisin, B., & Beckers, J.-M. (2011). *Introduction to geophysical fluid dynamics: Physical and numerical aspects* (2nd ed.). Academic Press.
- Davis, P. E. D., Lique, C., & Johnson, H. L. (2014). On the link between arctic sea ice decline and the freshwater content of the Beaufort Gyre: Insights from a simple process model. *Journal of Climate*, 27(21), 8170–8184. <https://doi.org/10.1175/JCLI-D-14-00090.1>
- Doddridge, E., & Radul, A. (2018). 'aronnax': An idealised isopycnal ocean model. *Journal of Open Source Software*, 3(26), 592. <https://doi.org/10.21105/joss.00592>
- Ghaffari, P., Isachsen, P. E., Nøst, O. A., & Weber, J. E. (2018). The influence of topography on the stability of the Norwegian Atlantic Current off Northern Norway. *Journal of Physical Oceanography*, 48(11), 2761–2777. <https://doi.org/10.1175/jpo-d-17-0235.1>
- Gill, A. (1968). A linear model of the Antarctic Circumpolar Current. *Journal of Fluid Mechanics*, 32(3), 465–488. <https://doi.org/10.1017/s0022112068000868>
- Gill, A. E., Green, J. S. A., & Simmons, A. J. (1974). Energy partition in the large-scale ocean circulation and the production of mid-ocean eddies. *Deep-Sea Research*, 21(7), 499–528. [https://doi.org/10.1016/0011-7471\(74\)90010-2](https://doi.org/10.1016/0011-7471(74)90010-2)
- Isachsen, P. E., Koszalka, I., & LaCasce, J. H. (2012). Observed and modeled surface eddy heat fluxes in the eastern Nordic Seas. *Journal of Geophysical Research*, 117(C8), 1–10. <https://doi.org/10.1029/2012JC007935>
- Isachsen, P. E., & Nøst, O. A. (2012). The air-sea transformation and residual overturning circulation within the Nordic Seas. *Journal of Marine Research*, 70(1), 31–68. Retrieved from https://elischolar.library.yale.edu/journal_of_marine_research/332/
- Isachsen, P. E., Vogt-Vincent, N., Johnson, H., & Nilsson, J. (2023). Supplementary datasets and code for: Instability and mesoscale eddy fluxes in an idealized 3-layer Beaufort Gyre. *Zenodo*. <https://doi.org/10.5281/ZENODO.10152749>
- Jansen, M., & Ferrari, R. (2012). Macroturbulent equilibration in a thermally forced primitive equation system. *Journal of the Atmospheric Sciences*, 69(2), 695–713. <https://doi.org/10.1175/JAS-D-11-041.1>
- Johnson, G. C., & Bryden, L. H. (1989). On the size of the Antarctic Circumpolar Current. *Deep-Sea Research*, 36(1), 39–55. [https://doi.org/10.1016/0198-0149\(89\)90017-4](https://doi.org/10.1016/0198-0149(89)90017-4)
- Koszalka, I., LaCasce, J. H., Andersson, M., Orvik, K. A., & Mauritzen, C. (2011). Surface circulation in the Nordic Seas from clustered drifters. *Deep-Sea Research I*, 58(4), 468–485. <https://doi.org/10.1016/j.dsr.2011.01.007>
- Kubryakov, A. A., Kozlov, I. E., & Manucharyan, G. E. (2021). Large mesoscale eddies in the western Arctic Ocean from satellite altimetry measurements. *Journal of Geophysical Research: Oceans*, 126(5), e2020JC016670. <https://doi.org/10.1029/2020JC016670>
- Lindzen, R. S. (1993). Baroclinic neutrality and the tropopause. *Journal of the Atmospheric Sciences*, 50(8), 1148–1151. [https://doi.org/10.1175/1520-0469\(1993\)050<1148:bnatt>2.0.co;2](https://doi.org/10.1175/1520-0469(1993)050<1148:bnatt>2.0.co;2)
- Lique, C., Johnson, H. L., & Davis, P. E. D. (2015). On the interplay between the circulation in the surface and the intermediate layers of the Arctic Ocean. *Journal of Physical Oceanography*, 45(5), 393–1409. <https://doi.org/10.1175/JPO-D-14-0183.1>
- Lozier, M. S., & Reed, M. S. C. (2005). The influence of topography on the stability of shelfbreak fronts. *Journal of Physical Oceanography*, 35(6), 1023–1036. <https://doi.org/10.1175/jpo2717.1>
- Manucharyan, G. E., & Isachsen, P. E. (2019). Critical role of continental slopes in halocline and eddy dynamics of the Ekman-driven Beaufort Gyre. *Journal of Geophysical Research*, 124(4), 2679–2696. <https://doi.org/10.1029/2018JC014624>
- Manucharyan, G. E., & Spall, M. A. (2016). Wind-driven freshwater buildup and release in the Beaufort Gyre constrained by mesoscale eddies. *Geophysical Research Letters*, 43(1), 273–282. <https://doi.org/10.1002/2015GL065957>
- Manucharyan, G. E., Spall, M. A., & Thompson, A. F. (2016). A theory of the wind-driven Beaufort Gyre variability. *Journal of Physical Oceanography*, 46(11), 3263–3278. <https://doi.org/10.1175/jpo-d-16-0091.1>
- Manucharyan, G. E., & Stewart, A. L. (2022). Stirring of interior potential vorticity gradients as a formation mechanism for large subsurface-intensified eddies in the Beaufort Gyre. *Journal of Physical Oceanography*, 52, 3349–3370. <https://doi.org/10.1175/JPO-D-21-0040.1>
- Meneghello, G., Marshall, J., Cole, S. T., & Timmermans, M.-L. (2017). Observational inferences of lateral eddy diffusivity in the halocline of the Beaufort Gyre. *Geophysical Research Letters*, 44(12), 12331–12338. <https://doi.org/10.1002/2017GL075126>
- Meneghello, G., Marshall, J., Lique, C., Isachsen, P. E., Doddridge, E., Campin, J.-M., et al. (2021). Genesis and decay of mesoscale baroclinic eddies in the seasonally ice-covered interior Arctic Ocean. *Journal of Physical Oceanography*, 51(1), 115–129. <https://doi.org/10.1175/JPO-D-20-0054.1>
- Meneghello, G., Marshall, J., Timmermans, M.-L., & Scott, J. (2018). Observations of seasonal upwelling and downwelling in the Beaufort Sea mediated by sea ice. *Journal of Physical Oceanography*, 48(4), 795–805. <https://doi.org/10.1175/jpo-d-17-0188.1>
- Nøst, O. A., & Isachsen, P. E. (2003). The large-scale time-mean ocean circulation in the Nordic Seas and Arctic Ocean estimated from simplified dynamics. *Journal of Marine Research*, 61(2), 175–210. Retrieved from https://elischolar.library.yale.edu/journal_of_marine_research/7/
- Orvik, K. A., & Niiler, P. (2002). Major pathways of Atlantic water in the northern North Atlantic and Nordic Seas toward Arctic. *Geophysical Research Letters*, 29(19), 2-1–2-4. <https://doi.org/10.1029/2002GL015002>
- Proshutinsky, A., Bourke, R., & McLaughlin, F. (2002). The role of the Beaufort Gyre in Arctic climate variability: Seasonal to decadal climate scales. *Geophysical Research Letters*, 29(23), 15-1–15-4. <https://doi.org/10.1029/2002GL015847>
- Rhines, P. B. (1975). Waves and turbulence on a β -plane. *Journal of Fluid Mechanics*, 69(3), 417–443. <https://doi.org/10.1017/s0022112075001504>

- Rudels, A., & Carmack, E. (2022). Arctic Ocean water mass structure and circulation. *Oceanography*, 35, 52–65. <https://doi.org/10.5670/oceanog.2022.116>
- Salmon, R., Holloway, G., & Hendershott, M. (1976). The equilibrium statistical mechanics of simple quasi-geostrophic models. *Journal of Fluid Mechanics*, 75(4), 691–703. <https://doi.org/10.1017/s0022112076000463>
- Schneider, T., & Walker, C. C. (2006). Self-organization of atmospheric macroturbulence into critical states of weak nonlinear eddy–eddy interactions. *Journal of the Atmospheric Sciences*, 63(6), 1569–1586. <https://doi.org/10.1175/JAS3699.1>
- Schott, F., & Stommel, H. (1978). Beta-spirals and absolute velocities in different oceans. *Deep-Sea Research*, 25(11), 961–1010. [https://doi.org/10.1016/0146-6291\(78\)90583-0](https://doi.org/10.1016/0146-6291(78)90583-0)
- Schott, F., & Zantopp, R. (1980). On the effect of vertical mixing on the determination of absolute currents by the beta spiral method. *Deep-Sea Research*, 27(2), 173–180. [https://doi.org/10.1016/0198-0149\(80\)90095-3](https://doi.org/10.1016/0198-0149(80)90095-3)
- Scott, R., & Wang, F. (2005). Direct evidence of an oceanic inverse kinetic energy cascade from satellite altimetry. *Journal of Physical Oceanography*, 35(9), 1650–1666. <https://doi.org/10.1175/jpo2771.1>
- Segtnan, O. H., Furevik, T., & Jenkins, A. D. (2011). Heat and freshwater budgets of the Nordic Seas computed from atmospheric reanalysis and direct ocean observations. *Journal of Geophysical Research*, 116(C11), C11003. <https://doi.org/10.1029/2011JC006939>
- Smith, K. (2007). The geography of linear baroclinic instability in Earth's oceans. *Journal of Marine Research*, 65(5), 655–683. <https://doi.org/10.1357/002224007783649484>
- Spall, M. A. (2010). Non-local topographic influences on deep convection: An idealized model for the Nordic Seas. *Ocean Modelling*, 32(1–2), 72–85. <https://doi.org/10.1016/j.ocemod.2009.10.009>
- Sterl, M. F., LaCasce, J. H., Groeskamp, S., Nummelin, A., Isachsen, P. E., & Baatsen, M. L. J. (2024). Suppression of mesoscale eddy mixing by topographic PV gradients. *Journal of Physical Oceanography*, 54(5), 1089–1103. <https://doi.org/10.1175/JPO-D-23-0142.1>
- Stone, P. H. (1978). Baroclinic adjustment. *Journal of the Atmospheric Sciences*, 35(4), 561–571. [https://doi.org/10.1175/1520-0469\(1978\)035<0561:ba>2.0.co;2](https://doi.org/10.1175/1520-0469(1978)035<0561:ba>2.0.co;2)
- Timmermans, M.-L., & Marshall, J. (2020). Understanding Arctic Ocean circulation: A review of ocean dynamics in a changing climate. *Journal of Geophysical Research: Oceans*, 125(4), e2018JC014378. <https://doi.org/10.1029/2018JC014378>
- Trodahl, M., & Isachsen, P. E. (2018). Topographic influence on baroclinic instability and the mesoscale eddy field in the northern North Atlantic Ocean and the Nordic seas. *Journal of Physical Oceanography*, 48(11), 2593–2607. <https://doi.org/10.1175/JPO-D-17-0220.1>
- Tulloch, R., Marshall, J., Hill, C., & Smith, K. S. (2011). Scales, growth rates and spectral fluxes of baroclinic instability in the ocean. *Journal of Physical Oceanography*, 41(6), 1057–1076. <https://doi.org/10.1175/2011jpo4404.1>
- Vallis, G., & Maltrud, M. (1993). Generation of mean flows and jets on a beta plane and over topography. *Journal of Physical Oceanography*, 23(7), 1346–1362. [https://doi.org/10.1175/1520-0485\(1993\)023<1346:gomfaj>2.0.co;2](https://doi.org/10.1175/1520-0485(1993)023<1346:gomfaj>2.0.co;2)
- Vallis, G. K. (2017). *Atmospheric and oceanic fluid dynamics: Fundamentals and large-scale circulation* (2nd ed.). Cambridge University Press.
- Venaille, A. (2012). Bottom-trapped currents as statistical equilibrium states above topographic anomalies. *Journal of Fluid Mechanics*, 669, 500–510. <https://doi.org/10.1017/jfm.2012.146>
- Wang, Y., & Stewart, A. L. (2018). Eddy dynamics over continental slopes under retrograde winds: Insights from a model inter-comparison. *Ocean Modelling*, 121, 1–18. <https://doi.org/10.1016/j.ocemod.2017.11.006>
- Wang, Y., & Stewart, A. L. (2020). Scalings for eddy buoyancy transfer across continental slopes under retrograde winds. *Ocean Modelling*, 147, 101579. <https://doi.org/10.1016/j.ocemod.2020.101579>
- Ypma, S. L., Spall, M. A., Lambert, E., Georgiou, S., Pietrzak, J. D., & Katsman, C. A. (2020). The contrasting dynamics of the buoyancy-forced Lofoten and Greenland basins. *Journal of Physical Oceanography*, 50(5), 1227–1244. <https://doi.org/10.1175/JPO-D-19-0280.1>
- Zhang, J., & Steele, M. (2007). Effect of vertical mixing on the Atlantic Water layer circulation in the Arctic Ocean. *Journal of Geophysical Research*, 112(C4), C04S04. <https://doi.org/10.1029/2006JC003732>
- Zhao, M., Timmermans, M.-L., Cole, S. T., Krishfield, R., Proshutinsky, A., & Toole, J. M. (2014). Characterizing the eddy field in the Arctic Ocean halocline. *Journal of Geophysical Research: Oceans*, 119(12), 8800–8817. <https://doi.org/10.1002/2014JC010488>